Letter

# Orientational-induced strain hardening of axisymmetric grains

M. Amereh and B. Nadler*
*Department of Mechanical Engineering, University of Victoria, Victoria, British Columbia V8W 3P6, Canada*

(Received 28 March 2022; accepted 16 September 2022; published 3 October 2022)

The rheological response of oriented axisymmetric grains has additional degrees of complexity associated with their microstructure orientation. These additional kinematic degrees of freedom that give rise to complex transient macroscale rheological responses are not well understood. In this Letter, we study the rheology of axisymmetric grains subjected to transient flow. We identify strong coupling between the microstructure rearrangement and strain hardening which, under certain conditions, can yield jamming. We identify the critical conditions corresponding to jamming and the dependency on the shape of the grains. It is shown that this is a particular form of jamming that is directional in nature, since unjamming occurs if the shear direction is reversed.

DOI: 10.1103/PhysRevE.106.L042901

Aspherical axisymmetric grains are abundant in nature and industry including agriculture, food processing, and pharmaceutics, however, their rheological properties are not well understood [1]. The orientation of these grains and their tendency to align with the flow add an additional element of complexity to such systems. The orientation and alignment of these grains depend on the flow and the shape of the grains, which couples the flow and the orientation through the rheological response. The microstructure orientation of axisymmetric grains plays an important role in their macroscale rheological responses in the form of strain hardening/softening and under certain conditions, that are identified in this Letter, jamming.

The steady state orientation of axisymmetric grains subjected to a simple shear flow has been extensively studied in recent years [2–8], however, the transient response is much less understood. In steady state simple shear flow, it was observed [6,7], using the discrete element method (DEM), that the grains with a higher degree of asphericity tend to align more with the flow and with respect to each other, which, in turn, reduces the shear flow resistance along the alignment planes. However, the transient shear-reversal response of axisymmetric grains activates a microstructure rearrangement with respect to the flow, which increases shear flow resistance and gives rise to strain hardening [9–12]. To obtain a realistic understanding of this microstructural effect, advanced models that account explicitly for the microstructure are needed.

If, due to strain hardening, the critical shear flow resistance exceeds the applied shear traction, the flow undergoes jamming [13–23]. Although the rheology of granular flows close to jamming has been studied with a focus on packing fractions and the number of contacts per particle [24–30], the role of microstructure orientation, that is the focus of this Letter, is less investigated. This Letter extends results from earlier studies of steady state flows to transient flow where significant microstructure changes develop. To understand this complex response, we study the transient rheological response of axisymmetric grains to shear reversal and establish a relationship between the microstructure configuration and the critical shear resistance. Importantly, we find that the transient rheological response strongly depends on the shape of the axisymmetric grains. The anisotropic inertia rheology [31] has the form

$$\boldsymbol{\sigma} = -p\mathbf{I} + p\mu(I)[\bar{\mathbf{D}} - \eta(\mathbf{A}\bar{\mathbf{D}} + \bar{\mathbf{D}}\mathbf{A} - 2/3(\bar{\mathbf{D}}\cdot\mathbf{A})\mathbf{I})], \quad (1)$$

where $\boldsymbol{\sigma}$ is the Cauchy stress, $p$ is the pressure, $\bar{\mathbf{D}} = \mathbf{D}/D$ is the direction of the rate of deformation $\mathbf{D}$, $D = \sqrt{2\mathbf{D}\cdot\mathbf{D}}$ is the magnitude of the rate of deformation, $\mathbf{A}$ is the orientational tensor that accounts for the microstructure orientation of the grains, $\mu(I) = \mu_s + \mu_1 I^{\beta}$ is the inertia rheology, $\mu_s$, $\mu_1$, $\beta$ are the rheology parameters, $I = Dd/\sqrt{p/\rho_s}$ is the inertia number, and $d$ and $\rho_s$ are the dimension and the density of the solid grains, respectively. The phenomenological parameters $\mu_s$, $\mu_1$, $\beta$, and $\eta$ are related to the grains' shape and the interfacial friction, where $\eta$ accounts for an anisotropic rheology that gives rise to a reduction in the shear flow resistance along the alignment planes.

The orientational tensor is a macroscale measure representing the microstructure orientation of the grains $\mathbf{A} = \oint_{S^2} f(\mathbf{k})\mathbf{k}\otimes\mathbf{k}\,da$, where $f(\mathbf{k})$ is the orientation probability density function in the direction $\mathbf{k}$ and $S^2$ is the 2-sphere. The evolution law for the orientational tensor [32,33] when subjected to flow is

$$\mathring{\mathbf{A}} = \dot{\mathbf{A}} + \mathbf{A}\mathbf{W} - \mathbf{W}\mathbf{A} = \lambda[\mathbf{A}\mathbf{D} + \mathbf{D}\mathbf{A} - 2[\mathbf{A}\cdot\mathbf{D}]\mathbf{A}] - \psi D'[\mathbf{A} - \mathbf{I}/3] + \mathrm{div}\,[\alpha D'\,\mathrm{grad}\,\mathbf{A}], \quad (2)$$

where $\mathring{\mathbf{A}}$ and $\dot{\mathbf{A}}$ are the objective Green-Naghdi rate and the time derivative of the orientational tensor, respectively, $\mathbf{W}$ is the vorticity tensor, $\mathbf{D}' = \mathbf{D} - (\mathbf{D}\cdot\mathbf{I})\mathbf{I}/3$ is the deviatoric part of the rate of deformation, and $D' = \sqrt{2\mathbf{D}'\cdot\mathbf{D}'}$ is its magnitude. The phenomenological model parameters $\lambda$, measuring the tendency of the particles to align with the

*bnadler@uvic.ca

 

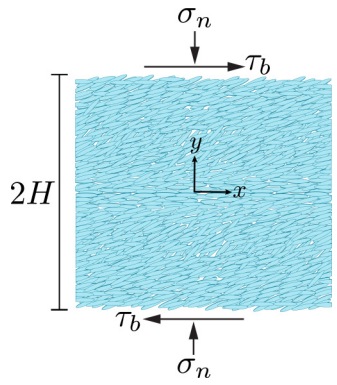


FIG. 1. Schematic representation of axisymmetric grain flow subjected to shear traction $\tau_b$ and normal traction $\sigma_n$.

flow, and $\psi$, measuring the relaxation toward isotropic orientation, were determined from DEM simulations of steady state shear flow [32], and $\alpha$ is the orientation diffusion coefficient. The conservation of mass and the balance of linear momentum are

$$\dot{\rho} + \rho \operatorname{div} \mathbf{v} = 0, \quad \rho \dot{\mathbf{v}} = \rho \mathbf{b} + \operatorname{div} \boldsymbol{\sigma}, \tag{3}$$

where $\rho$ is the density, $\mathbf{v}$ is the velocity, and $\mathbf{b}$ is the body force.

The study of the rheological response of axisymmetric grains at steady state shear flow is limited to a single microstructure configuration which is associated with relatively high microstructure ordering and alignment with the flow. To advance our understanding of the role of the microstructure on the macroscale rheological response, it is necessary to study a range of microstructure configurations. The objective of this Letter is to explore the rheological properties under different microstructure configurations and to obtain an understanding of their coupling. During shear reversal, as the system evolves from one steady state to the inverted steady state, the microstructure rearranges through a continuous sequence of configurations, and by exploring the associated rheological properties we are able to discover this relationship. This motivates the study of shear reversal of axisymmetric grains as depicted in Fig. 1. At steady state shear flow, it is well known [2–4,6,32] that the grains obtain a highly ordered microstructure configuration which is aligned with the flow, which yields low shear flow resistance. However, during shear reversal, the instantaneous reversal of the direction of shear activates a microstructure rearrangement. During this transient process, the grains go through continuously evolving configurations from high to low and back to high ordered configurations and alignment with the flow at the new steady state [18,32]. These intermediate disordered configurations give rise to an increase in the shear flow resistance followed by a decrease. On the macroscale, this manifests strain hardening, which in turn decelerates the flow and has the potential to induce jamming, followed by strain softening where the flow accelerates as the system returns to a highly ordered and aligned configuration at steady state. The return to the steady state occurs only if the system does not undergo jamming during the process.

To obtain meaningful insight into the transient rheological response, we neglect inertia effects and body forces, by setting $\rho = 0$ and $\mathbf{b} = \mathbf{0}$, and we only consider the bulk response far enough from boundaries to eliminate boundary effects. Shear reversal is obtained by instantaneously reversing the direction of the applied shear traction $\tau_b$ while maintaining the same magnitude. Considering uniform conditions in the $x$ and $z$ directions, the velocity, pressure, and orientation tensor are only functions of the height $y$ and time $t$, i.e., $\mathbf{v} = v(y,t)\boldsymbol{i}$, $p(y,t)$, $\mathbf{A}(y,t)$. It follows that the rate of deformation and the vorticity take the forms $\mathbf{D} = \dot{\gamma}(\boldsymbol{i} \otimes \boldsymbol{j} + \boldsymbol{j} \otimes \boldsymbol{i})/2$ and $\mathbf{W} = \dot{\gamma}(\boldsymbol{i} \otimes \boldsymbol{j} - \boldsymbol{j} \otimes \boldsymbol{i})/2$, respectively, where $\dot{\gamma} = \partial v/\partial y$ is the shear rate. The flow is isochoric since $\operatorname{div} \mathbf{v} = 0$ which is consistent with the incompressibility of the inertia rheology (1). The conservation of mass is satisfied for $\rho = \text{const}$, and the pressure $p$ is a Lagrangian multiplier. The field variables, velocity $v$, pressure $p$, and the orientational tensor $\mathbf{A}$, are governed by the balance of linear momentum, second equation in (3), supplemented by the anisotropic inertia rheology (1) and the evolution of the orientational tensor (2). The loadings and orientational fluxes at the edges are

$$\sigma_{yy} = -\sigma_n, \quad \sigma_{xy} = \tau_b, \quad \partial \mathbf{A}/\partial y = \mathbf{0} \quad \text{at } y = \pm H. \tag{4}$$

The steady state configuration, i.e., $\dot{\mathbf{A}} = \mathbf{0}$ and $\dot{v} = 0$, is taken as the initial configuration when the shear -reversal is applied. The model parameters are given by Refs. [32] and [31] as

$$\lambda(r_g) = (2/\pi)\tan^{-1}(5.5 r_g),$$
$$\psi(r_g) = 0.85 \exp\left(-4 r_g^2\right), \quad \eta(r_g) = 0.746 \tan^{-1}(4.266 |r_g|), \tag{5}$$

where $r_g = (l-d)/(l+d)$ is the aspect ratio of axisymmetric grains of length $l$ and diameter $d$. This set of parameters was determined by DEM simulations of steady state shear flow [7,32]. The parameters $\lambda$ and $\psi$ govern the orientation of grains, predicting that, at steady state, the grains with higher asphericity tend to have higher order and alignment with the shear flow. The parameter $\eta$ governs the anisotropic rheological response, predicting that the higher alignment of the axisymmetric grains with the flow leads to lower shear flow resistance along the planes of alignment.

The dependency of the shear flow resistance on the microstructure configuration gives rise to a complex rheological response during transient shear reversal due to the associated rearrangement of the microstructure. By the anisotropic rheological model (1), the developed shear stress is

$$\tau = |\sigma_{xy}| = p\mu(I)(1 - \eta A_p), \quad A_p = A_{xx} + A_{yy}, \tag{6}$$

and the significance of this expression is that we obtained an expression for the dependency of shear flow resistance, along the $x$-$y$ plane, on the orientational tensor $\mathbf{A}$ which is through $A_p$. It follows that the critical shear flow resistance when approaching jamming, i.e., $I \to 0$ and hence $\mu(I) \to \mu_s$, is

$$\tau_{\text{cr}} = p\mu_s(1 - \eta A_p), \tag{7}$$

which presents an explicit jamming criterion. Therefore, shear traction $\tau_b$, lower than the shear flow resistance $\tau_b < \tau_{\text{cr}}$, necessarily yields jamming. It was observed [32] that during shear

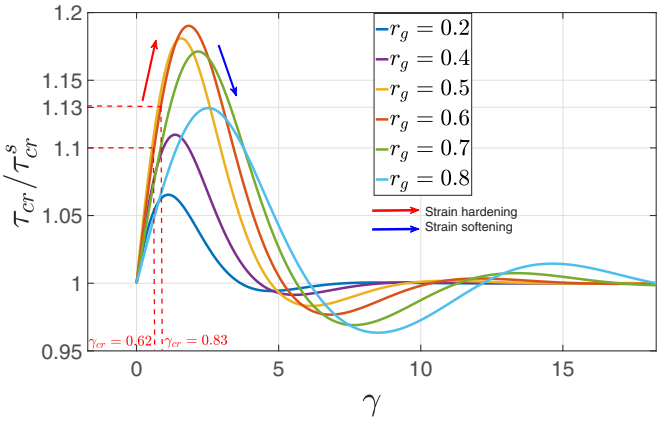


FIG. 2. Evolution of the critical shear $\tau_{\rm cr}$, normalized by the steady state critical shear $\tau^s_{\rm cr}$, during shear reversal for a range of aspect ratios $r_g$. The maximum strain hardening occurs for $r_g = 0.6$. The critical shear strains $\gamma_{\rm cr} = \{0.62, 0.83\}$ associated with $\tau_{\rm cr}/\tau^s_{\rm cr} = \{1.1, 1.13\}$ are marked on the figure.

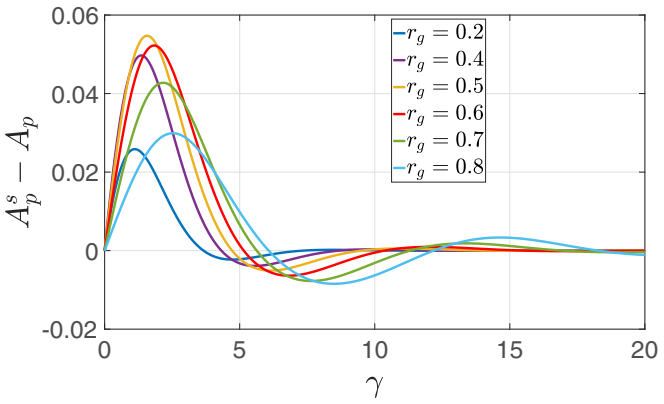


FIG. 3. Evolution of the shear ordering $A_p$, with respect to the steady state $A^s_p$, during shear reversal for various aspect ratios $r_g$. The maximum decrease in shear ordering corresponds to $r_g = 0.5$–$0.6$.

reversal the microstructure rearrangement initially yields an increase in the disorder before returning to a higher ordered configuration at steady state. This process of rearrangement and the initial increase of microstructure disorder give rise to strain hardening and an increase of the critical shear flow resistance $\tau_{\rm cr}$, which induces possible jamming as was observed in Ref. [18].

To investigate the evolution of the critical shear resistance during shear reversal, we simulate the evolution of the orientational tensor (2) and the associated critical shear resistance (7). The simulations start at steady state activating shear reversal by inverting the direction of the applied shear traction $\tau_b$. We apply sufficient shear traction to assure that jamming does not occur and the shear-reversal process is completed. Figure 2 depicts the deviation of the ratio of the critical shear $\tau_{\rm cr}$ to the steady state critical shear $\tau^s_{\rm cr}$ versus the shear strain $\gamma = \int_0^t \dot\gamma dt$. The overall shear rate $\dot\gamma$ is the difference between the velocities of the top and bottom layers divided by the flow thickness, $\dot\gamma = [v(H,t) - v(-H,t)]/[2H]$.

Figure 2 depicts the variation of the critical shear flow resistance, starting with a strain hardening (red arrow), followed by a strain softening (blue arrow), as the microstructure returns to the ordered configuration. The bulk part of the shear reversal is completed at $\gamma \approx 5$, which is consistent with the two-dimensional DEM simulations of shear reversal presented in Ref. [18]. However, steady state is obtained only after $\gamma \approx 12$–$20$, which depends on the aspect ratio $r_g$ of the grains. Interestingly, the strain hardening has a nonmonotonic dependency on the aspect ratio. The maximum strain hardening of 19% corresponds to $r_g = 0.6$, while for other aspect ratios it is less significant and can be as low as 6%. This nonmonotonic response is contributed to the different microstructure rearrangement processes during shear reversal of grains of different aspect ratios.

The microstructure orientation measure that governs the shear flow resistance is the shear ordering $A_p$, as implied by Eq. (7). Figure 3 shows the evolution of $A_p$ with respect to the steady state $A^s_p$ versus the shear strain during shear reversal. It can be seen that the maximum decrease in shear ordering indeed corresponds to $r_g = 0.5$–$0.6$. This is expected as it is known [6,32] that for small $r_g$ the grains are not well ordered and aligned with the flow even at steady state, therefore, shear reversal yields a relatively insignificant change to the ordering and alignment and, as a result, to the critical shear flow resistance. On the other hand, for large $r_g$, the grains are highly ordered and aligned with the flow at steady state, and they maintain it during shear reversal which yields only a small increase to the critical shear flow resistance. Consequently, the rheological response to shear reversal is relatively mild for $r_g < 0.4$ and $r_g > 0.7$, and is most significant for $r_g = 0.6$. Figure 3 provides a microstructural justification to the macroscale rheological response in Fig. 2.

Next, we focus on the eminent case of $r_g = 0.6$, which undergoes the most significant strain hardening, to study jamming and unjamming. Inspection of Fig. 2 suggests that for $r_g = 0.6$, during shear reversal, the critical shear flow resistance increases to the maximum value of $\tau^{\rm max}_{\rm cr} = 1.19\tau^s_{\rm cr}$ and decreases to the minimum value $\tau^{\rm min}_{\rm cr} = 0.98\tau^s_{\rm cr}$. Hence, given that the applied shear traction is $\tau_b > \tau^{\rm max}_{\rm cr}$, the system exhibits strain hardening, but jamming does not arise. However, for applied shear traction lower than the maximum critical shear flow resistance, but larger than the steady state critical shear flow resistance, to maintain steady state shear flow, $\tau^s_{\rm cr} < \tau_b < \tau^{\rm max}_{\rm cr}$, strain hardening occurs. It increases the critical shear flow resistance and decelerates the flow until the critical shear flow resistance reaches the applied shear traction. At this point the flow stops and jamming takes effect.

To investigate the jamming and unjamming processes, we also applied a second shear reversal after jamming takes effect to drive the system to resume flow. The evolution of this process is shown in Fig. 4, where time $t$ is normalized with respect to the timescale of the system $\hat t = t\sqrt{\sigma_n/\rho_s}/H$. Given a steady state shear flow, the direction of the shear traction is instantly reversed at $\hat t = 0$. After jamming takes effect, a second shear reversal is applied at $\hat t_1$. Figure 4 depicts the rate of shear $\dot\gamma$ and the shear strain $\gamma$ as a function of the normalized time for $\tau_b < \tau^{\rm max}_{\rm cr}$. As expected, at the activation of shear reversal, $\hat t = 0$, strain hardening is initiated and the flow decelerates. Since $\tau_b < \tau^{\rm max}_{\rm cr}$, jamming occurs at $\hat t \approx 400$, then the flow

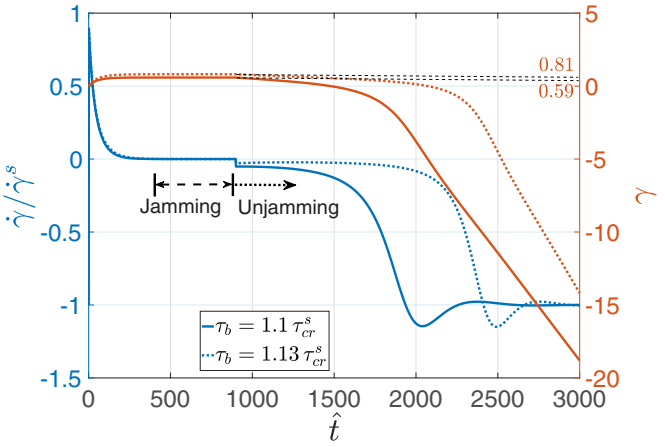


FIG. 4. The rate of shear $\dot{\gamma}$ and shear strain $\gamma$ vs time during double shear reversal for $r_g = 0.6$ and applied shear traction below the critical shear resistance, $\tau_b = \{1.1, 1.13\}\tau^s_{\rm cr} < \tau^{\rm max}_{\rm cr}$. The corresponding critical strains $\gamma_{\rm cr} = \{0.59, 0.81\}$ are also marked in Fig. 2.

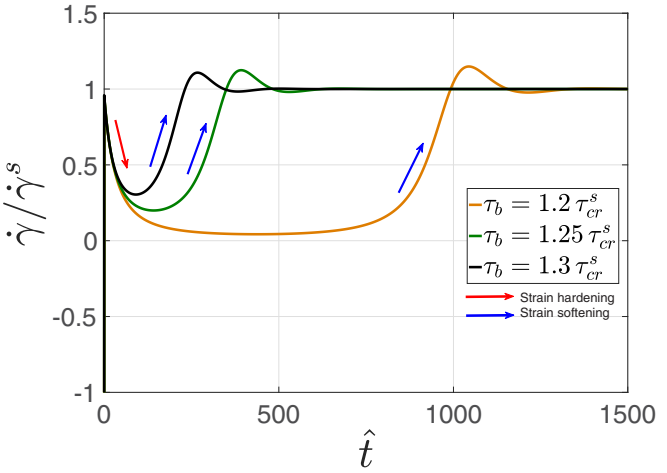


FIG. 5. The rate of shear $\dot{\gamma}$ vs time during shear reversal for $r_g = 0.6$ and applied shear traction above the critical shear resistance, $\tau_b = \{1.2, 1.25, 1.3\}\tau^s_{\rm cr} > \tau^{\rm max}_{\rm cr}$. The flow experiences a strain hardening followed by a strain softening and eventually returns to steady state flow. The higher applied shear traction yields the faster return to steady state flow.

stops. Figure 4 shows that for $\tau_b = \{1.1, 1.13\}\tau^s_{\rm cr}$ jamming is obtained at $\gamma = \{0.59, 0.81\}$, respectively, which is consistent with Fig. 2, where the shear strains at jamming approach the expected values $\gamma_{\rm cr} = \{0.62, 0.83\}$. As the critical shear resistance approaches from below the applied shear traction $\tau_{\rm cr} \to \tau_b$ and so does the shear strain $\gamma \to \gamma_{\rm cr}$, the shear rate decreases toward zero, $\dot{\gamma} \to 0$, until jamming takes effect. Figure 4 also shows that when the second shear reversal is applied at $\hat{t}_1 = 900$ to the jammed system, unjamming occurs immediately, followed by strain softening as the shear strain $\gamma$ decreases. Similar jamming and unjamming responses were also observed in Ref. [18] using two-dimensional DEM simulations. Figure 4 shows that for the two applied shear traction cases, $\tau_b = \{1.1, 1.13\}\tau^s_{\rm cr}$, the jamming processes are very similar with respect to time, but occur at different strains. However, the unjamming processes are different with respect to time as the unjamming of $\tau_b = 1.13\tau^s_{\rm cr}$ takes longer than $\tau_b = 1.1\tau^s_{\rm cr}$ to return to the steady state. This response is attributed to the larger strain hardening obtained at jamming for the larger applied traction, and therefore the system requires a longer time to return to steady state flow. It should be noted that the overshooting of the strain softening at the end of the shear-reversal process just before returning to the steady state may be attributed to the inertia of the evolution process where, for a short period, the system obtains a highly oriented and aligned configuration before returning to a less oriented and aligned configuration at the steady state. This response was not observed in the two-dimensional DEM simulation of shear reversal [18], however, orientational overshooting was observed in three-dimensional DEM simulations [32]. Hence, we believe that this is a three-dimensional effect, where grains can orient in the out-of-plane direction, rather than a deficiency of the model (2).

To demonstrate that $\tau_b > \tau^{\rm max}_{\rm cr}$ does not induce jamming, the shear-reversal responses for $\tau_b = \{1.2, 1.25, 1.3\}\tau^s_{\rm cr}$ are depicted in Fig. 5. It can be observed that jamming does not occur even though the strain hardening yields a significant decrease in shear rate, particularly for $\tau_b = 1.2\tau^s_{\rm cr}$ as the applied shear traction is very close to but above the critical shear resistance. As can be seen in Fig. 5, following an initial strain hardening, strain softening occurs and flow accelerates until the shear-reversal process is completed and the system returns to steady state flow. As expected, the larger the applied traction, the faster the shear-reversal process is completed.

In summary, we study the transient response of axisymmetric grains subjected to shear reversal using the anisotropic inertia rheology and orientation evolution model. It is demonstrated that the highly ordered configuration of grains at steady state flow, which has a relatively low shear flow resistance, undergoes a microstructural rearrangement when subjected to shear reversal. This rearrangement leads to a reduced order configuration which gives rise to macroscale strain hardening, and hence to flow deceleration. We identify the shear flow resistance dependency on the microstructure which describes the macroscale response of this complex process and provides criteria for orientational-induced jamming. The subsequent increase in the shear flow resistance can induce jamming if the applied shear traction is insufficient to overcome the strain hardening. However, for large enough applied shear traction, no jamming occurs and the microstructure resumes highly ordered configurations. If the applied shear traction is insufficient to overcome the strain hardening, jamming occurs. We have also shown that when a shear reversal is applied to a jammed system, unjamming takes effect and flow resumes as strain softening occurs.

Support from the National Science and Engineering Research Council of Canada (NSERC, Grant No. RGPIN-2018-04573) is gratefully acknowledged.

[1] P. W. Cleary and M. L. Sawley, Appl. Math. Model. **26**, 89 (2002).
[2] T. Börzsönyi, B. Szabó, G. Törös, S. Wegner, J. Török, E. Somfai, T. Bien, and R. Stannarius, Phys. Rev. Lett. **108**, 228302 (2012).
[3] S. Wegner, T. Börzsönyi, T. Bien, G. Rose, and R. Stannarius, Soft Matter **8**, 10950 (2012).
[4] D. Berzi, N. Thai-Quang, Y. Guo, and J. Curtis, Phys. Rev. E **93**, 040901(R) (2016).
[5] D. Berzi, N. Thai-Quang, Y. Guo, and J. Curtis, Phys. Rev. E **95**, 050901(R) (2017).
[6] M. Trulsson, J. Fluid Mech. **849**, 718 (2018).
[7] D. B. Nagy, P. Claudin, T. Börzsönyi, and E. Somfai, Phys. Rev. E **96**, 062903 (2017).
[8] Y. Guo, C. Wassgren, W. Ketterhagen, B. Hancock, B. James, and J. Curtis, J. Fluid Mech. **713**, 1 (2012).
[9] N. Y. C. Lin, B. M. Guy, M. Hermes, C. Ness, J. Sun, W. C. K. Poon, and I. Cohen, Phys. Rev. Lett. **115**, 228304 (2015).
[10] R. Seto, R. Mari, J. F. Morris, and M. M. Denn, Phys. Rev. Lett. **111**, 218301 (2013).
[11] M. Wyart and M. E. Cates, Phys. Rev. Lett. **112**, 098302 (2014).
[12] J. Dong and M. Trulsson, Phys. Rev. Fluids **2**, 081301(R) (2017).
[13] F. Gadala-Maria and A. Acrivos, J. Rheol. **24**, 799 (1980).
[14] M. E. Cates, J. P. Wittmer, J.-P. Bouchaud, and P. Claudin, Phys. Rev. Lett. **81**, 1841 (1998).
[15] D. Bi, J. Zhang, B. Chakraborty, and R. P. Behringer, Nature (London) **480**, 355 (2011).
[16] P. Olsson, Phys. Rev. Lett. **122**, 108003 (2019).
[17] R. Seto, A. Singh, B. Chakraborty, M. M. Denn, and J. F. Morris, Granular Matter **21**, 82 (2019).
[18] M. Trulsson, Phys. Rev. E **104**, 044614 (2021).
[19] C. Heussinger and J.-L. Barrat, Phys. Rev. Lett. **102**, 218303 (2009).
[20] M. Otsuki and H. Hayakawa, Phys. Rev. E **83**, 051301 (2011).
[21] T. Hatano, J. Phys. Soc. Jpn. **77**, 123002 (2008).
[22] S. Henkes, M. van Hecke, and W. van Saarloos, Europhys. Lett. **90**, 14003 (2010).
[23] G. G. Giusteri and R. Seto, Phys. Rev. Lett. **127**, 138001 (2021).
[24] L. E. Silbert, Soft Matter **6**, 2918 (2010).
[25] A. Donev, I. Cisse, D. Sachs, E. A. Variano, F. H. Stillinger, R. Connelly, S. Torquato, and P. M. Chaikin, Science **303**, 990 (2004).
[26] A. Donev, R. Connelly, F. H. Stillinger, and S. Torquato, Phys. Rev. E **75**, 051304 (2007).
[27] T. Marschall and S. Teitel, Phys. Rev. E **97**, 012905 (2018).
[28] C. F. Schreck, N. Xu, and C. S. O'Hern, Soft Matter **6**, 2960 (2010).
[29] T. Majmudar, M. Sperl, S. Luding, and R. P. Behringer, Phys. Rev. Lett. **98**, 058001 (2007).
[30] L. E. Silbert, A. J. Liu, and S. R. Nagel, Phys. Rev. Lett. **95**, 098301 (2005).
[31] B. Nadler, Granular Matter **23**, 14 (2021).
[32] B. Nadler, F. Guillard, and I. Einav, Phys. Rev. Lett. **120**, 198003 (2018).
[33] M. Amereh and B. Nadler, J. Fluid Mech. **936**, A40 (2022).